Journal of Catalysis **201,** 275–285 (2001)
doi:10.1006/jcat.2001.3261, available online at http://www.idealibrary.com on IDEAL®

CO Oxidation Bistability Diagrams for Pt/CeO_x and Pt/SiO_2 Model Catalysts Prepared by Electron-Beam Lithography

Stefan Johansson, Lars Österlund,[1] and Bengt Kasemo

Department of Applied Physics and Competence Centre for Catalysis, Chalmers University of Technology and Göteborg University, S-412 96, Göteborg, Sweden

Received March 1, 2001; accepted April 26, 2001

The CO oxidation bistability diagrams (i.e., the interval of gas mixing ratio $\beta \equiv P_{CO}/(P_{CO} + P_{O_2})$ vs temperature for which a bistability exists) have been determined for different electron beam lithography (EBL) fabricated supported model catalysts. Three different samples were studied, one Pt/SiO_2 sample and two Pt/CeO_x samples, where the support type, particle size, and interface length were varied independently. The kinetic bistability is an inherent property of the CO oxidation on Pt at certain gas mixtures and temperatures, and we find that the actual position of the bistable region is a very sensitive tool to measure differences in reaction kinetics on different samples. The bistable region is shifted considerably along the gas mixing ratio axis, β, between the three samples (at constant temperature). Simulations show that the experimental results can be understood by introducing an oxygen reactant supply via the CeO_x support (spillover), which does not exist for SiO_2. This extra supply of oxygen will maintain a high CO conversion rate up to higher relative CO partial pressures on ceria samples (by suppressing the CO poisoning effect). Energy barriers for O diffusion on CeO_x and the attachment across the Pt/CeO_x interface have been estimated. The formation of a less reactive Pt state under oxidizing conditions is discussed.

Key Words: **electron-beam lithography; Pt; CO oxidation; bistable reactions; kinetic phase transitions.**

1. INTRODUCTION

A modern automobile three-way exhaust catalyst (TWC) is capable of simultaneously oxidizing hydrocarbons, H_2 and CO, while at the same time reducing NO_x to N_2 by matching the fraction of reducing and oxidizing agents, respectively, in a narrow regime around stoichiometry (1, 2). This is achieved by an engine management system, which includes a solid-state oxygen sensor to monitor the oxygen content of the exhaust gas. Base-metal oxides are normally used as oxygen storage components in TWC catalysts to damp out rapid changes in the exhaust gas, i.e., to provide oxygen under rich conditions and store oxygen under lean conditions, hence facilitating a reasonable time response for the engine-exhaust feedback system. The choice of metal oxide depends on its ability to rapidly change oxidation states upon change in redox potential of the exhaust gas composition. The change in oxidation state is associated with the reversible removal of and addition of oxygen, hence the designation "oxygen storage" component. Ceria is by far the most commonly used oxygen storage component (1, 2), and there are numerous experimental and theoretical studies of the oxygen storage in ceria catalysts (3–7). The oxygen storage is commonly believed to occur via oxygen surface diffusion to and from the noble metal particle. The connection between experiments and calculations is, however, relatively weak, and, e.g., the surface diffusion of oxygen on ceria and the way oxygen is communicated between ceria and the catalyst particles, which are key parameters, are not well known. This is in part due to the complexity of the system, which prevents the use of many analytical tools otherwise employed in surface science studies on well-defined model systems.

There exist a number of different preparative approaches to bridge the structure gap between single crystals and supported catalysts. These include, e.g., vapor deposition (8–10), and cluster source methods (9, 11), both of which allow controlled preparation in vacuum. Others include spin coating (10, 12) and more recently, colloidal lithography (13) and microemulsion methods (14). A complementary approach, which we employ in the present study, is to use electron-beam lithography (EBL). In terms of simultaneous control over size, shape, and component interaction (e.g., particle–support) this technique is in general superior to many of the techniques mentioned above. We (15, 16) and others (17) have previously demonstrated the principal advantages of EBL for heterogeneous catalysis. (There are also limitations such as slow speed and relatively large minimum particle sizes). No study has, however, so far been reported which utilizes the full potential of EBL samples to systematically explore size and shape influences on the catalytic activity, or explore particle–support interactions. This is primarily due to the difficulties of producing sufficiently

[1] To whom correspondence should be addressed. E-mail: lars.osterlund@fy.chalmers.se.

0021-9517/01 $35.00

large arrays of particles that enable accurate measurements of reaction kinetics. We have recently solved this problem, at least partly, by the construction of a micro-flow reactor capable of studying EBL-samples well below 1 mm^2 of active particle surface area (18).

We exploit here the full functionality of EBL to prepare well-defined supported model catalysts to study a catalytic model reaction. We use the inherent kinetic bistability of the CO oxidation on Pt as a sensitive tool to monitor changes in the reaction kinetics. The bistable and oscillatory behavior of the CO oxidation on Pt at UHV conditions have been thoroughly studied both experimentally and theoretically (19–21). Corresponding studies performed at atmospheric conditions are less numerous (22–24), and atmospheric pressure studies with EBL fabricated samples have not before been reported. The origin of the bistability can be formulated quite generally (21). In the case of CO oxidation on Pt, it has its origin in the different adsorption kinetics for CO and O_2, respectively, where CO inhibits the (dissociative) adsorption of oxygen, but not vice versa. Simultaneously, the CO_2 desorption rate is rapid, so that no reaction products are present on the surface. Hence, in certain temperature and gas mixture intervals, a *bistable region* ($\beta_{\min}$ $\beta \equiv P_{CO}/(P_{CO} + P_{O_2})\beta_{\max}$) with two different stable solutions (and different steady state coverages) can be reached depending on the preceding history. Typically one solution is reached from the oxygen excess regime (high active state), and the other is reached from the CO excess regime (low active, or CO poisoned state). For such bistable cases, a bifurcation is observed in the reaction rate as the gas mixture is swept back and forth (in β) over the bistable region. Such a bifurcation occurs at constant temperature and should not be confused with catalytic ignition, for which a rapid increase in both reaction rate and temperature occurs when the Franck–Kamenetskii condition is fulfilled, i.e., the point where the chemical power generated by the exothermic reaction is no longer balanced by the heat conducted away from the Pt particle (25). The bifurcation mentioned above is a kinetic phase transition and is due to sudden changes in the reaction kinetics on the surface only, and can occur even without an increase in temperature. Zhdanov and Kasemo (26) have shown that the regimes of such bifurcations can be shifted (in β) if surface diffusion of reactants from the support to the active surface is included in the simulations. In the present study, we take an experimental approach to measure the bistable reaction regions for Pt/ceria and Pt/silica using EBL model catalysts. We show that differences in the surface kinetics (caused by the different supports) are readily detected with our experimental approach. Mean-field simulations, including an extra reactant channel of oxygen surface diffusion on ceria toward Pt, explain the results, and provide a detailed understanding of the role of surface oxygen in Pt/ceria catalysts.

2. EXPERIMENTAL

2.1. Electron-Beam Lithography (EBL) Fabricated Model Catalysts

The EBL fabrication method has been used to prepare Pt/CeO_x and Pt/SiO_2 model catalysts. The preparation procedure is in short as follows. To produce a SiO_2 support, a Si wafer is thermally oxidized to produce a 100-nm thick SiO_2 layer. This is followed by cleaning in a reactive ion etching (RIE) oxygen plasma (250 W, 50 Torr O_2, 120 s). To prepare the CeO_x support, a 30-nm thick CeO_x layer is deposited on top of the SiO_2 layer by electron beam evaporation (0.5 Å/s) of a CeO_2 target in an AVAC HVC-600 thin film deposition system. The support grown in this way is most probably nonsaturated CeO_x ($x < 2$). A resist layer consisting of Zep 7000B is deposited on the wafer by spin-coating (to 300 nm thickness) and is subsequently baked at 170°C for 20 min. The resist is exposed to the prescribed pattern in an electron beam lithography system (JEOL JBX-5DII). Development of the resist is then made in a solution of Methylethylketon (MEK) : Diethylemalonate (1 : 1) for 3–5 min and subsequent rinsing in isopropanol. A soft RIE oxygen plasma treatment (50 W, 10 Torr O_2, 30 s) is made before depositing Pt by electron beam evaporation in the AVAC HVC-600 system. Lift-off is made in a MEK solution at 42°C (held in an ultrasonic bath). The projected geometrical Pt surface area is determined to be 0.4 mm^2 for all samples,and consists of large arrays of 750 nm in diameter Pt particles situated on the support with a center-to-center spacing of 1400 nm (Fig. 1). The EBL samples prepared in this manner are chemically well defined as determined by AES and ESCA analysis. Three samples have been studied: Pt/SiO_2 (I), Pt/CeO_x (II), Pt/CeO_x (III). The samples have been pretreated at different temperatures (I $\leftrightarrow$ 673 K, II $\leftrightarrow$ 573 K, and III $\leftrightarrow$ 748 K) in a 0.5% H_2 + 1.0% O_2 mixture diluted in Ar for 10 h each. Sample III has in addition been treated in a 0.87% H_2 + 0.63% O_2 mixture diluted in Ar for an additional 10 h at the same temperature. These pretreatments have been made in order to stabilize the samples at a higher temperature than was used during the catalytic reaction experiments. The possibility of a small amounts of intermixing of the CeO_x with the underlying SiO_2 oxide cannot, however, be ruled out after these pretreatments, especially for sample III. For sample III, the pretreatment results in a reaction-induced reconstruction and disintegration of the Pt particles into smaller particles (see Fig. 1c), as previously described at a somewhat higher temperature (15). This procedure has been adopted to prepare a Pt/CeO_x sample with very different particle size from the same batch of 750 nm Pt/CeO_x samples. The smaller particles are situated in the area previously occupied by the original particle, so the original array pattern is still visible. The smaller particles have a mean "diameter" of approximately 200 nm, as estimated from SEM

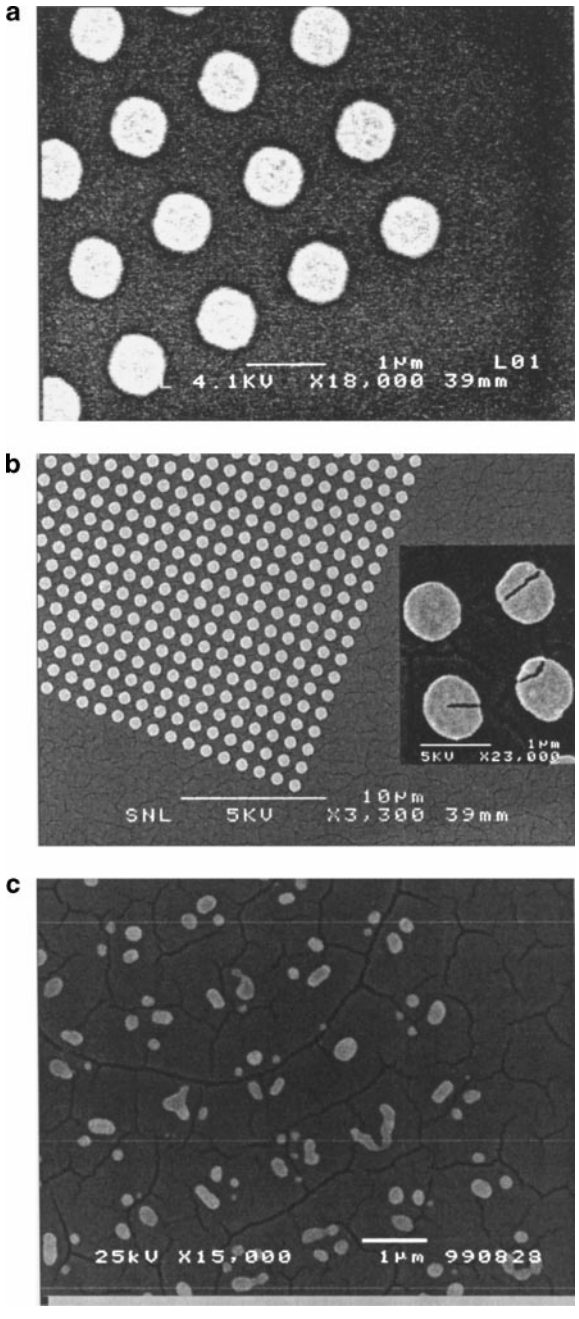

FIG. 1. SEM pictures of EBL-fabricated (a) Pt/SiO_2 and ((b) and (c)) Pt/CeO_x samples. In (a) and (b) the particle size is 750 nm in diameter, 20 nm in height, and the center-to-center distance between particles is 1400 nm. The inset in (b) shows a few particles from the larger array. In (c) such particles have disintegrated by heat treatments at 748 K in H_2+O_2 mixtures diluted in Ar.

images. In the following we denote these samples as 200 nm Pt/CeO_x. The geometrical surface area of sample III has decreased by almost a factor of 4 during the pretreatment, compared with the other two samples. The details of this Pt loss mechanism will not be discussed here, but it is worth noting that an actual decrease of surface Pt sites by about a factor of 4 (which cannot be explained by particle reshaping) is confirmed also by the simulations discussed in Section 4.

2.2. Micro-flow Reactor

The micro-flow reactor used for catalytic activity measurements has been described elsewhere (19). In short, the micro-flow reactor consists of long inlet and outlet channels (100 mm) with small inner diameters (0.1 and 0.2 mm, respectively). The micro-flow reactor is situated inside an evacuated quartz tube equipped with a capacitance manometer to monitor the pressure increase. The inlet and outlet of the micro-flow reactor are connected to a flow bypass and to a mass spectrometer, respectively. The total flow through the micro-flow reactor is set up by two controlled flows, one from the outlet channel into a quadrupole mass spectrometer and one through a Pyrex seal from the micro-flow reactor into the evacuated quartz tube. The former leak is used to measure the gas composition in the reactor, while the latter seal is used for sample exchange. These two leak flows are in the same order of magnitude, and the total flow is approximately $\nu = 1$ μl/s. The reactor acts as a tank reactor with a gas resident time of about 100 s and a short mixing time through diffusion inside the reactor (in the range of seconds). Thus, we do not expect any gradients in the gas composition along the direction axial (i.e., the gas flow direction) of the reactor. The response time is long for a step-change in the gas feed (around 400 s), but moderate for depletion of reactants due to a fast reaction occurring on the catalyst sample inside the micro-flow reactor (tens of seconds). The thermocouple is attached to the outside of the micro-flow reactor. Heating of the reactor is accomplished by a heating coil outside the evacuated quartz tube, and a heat resistant fabric is shielding both the sample and the thermocouple from direct irradiation from the heating coil. Since the number of CO molecules are limited during full conversion to 175 ppm in a gas feed of 1 μl/s in the present study, the exothermic power generated during reaction is in the μW regime, giving a negligible temperature rise at the catalyst surface.

3. EXPERIMENTAL RESULTS

CO oxidation measurements were performed on EBL-fabricated Pt/CeO_x and Pt/SiO_2 model catalysts, and the bistable reaction regions for these samples, and their temperature dependence, have been mapped out. Within the bistability region there exist two steady state reaction rates for each gas composition in the gas phase. These two steady state reaction rates correspond to two branches, if plotted versus the β-parameter ($\beta \equiv P_{CO}/(P_{CO}+P_{O_2})$), and at each end of the bistability region there are discontinuous transitions in the reaction rate (kinetic phase transitions)

connecting the two branches. The branch which has the lowest reaction rate (the low rate branch) corresponds to a surface that is almost saturated with CO (CO-poisoned surface). The other branch (the high rate branch) can maintain a much higher reaction rate, since the surface coverage of CO is lower, allowing oxygen to adsorb and react on the surface, and thereby creating new adsorption sites, where CO and O_2 can adsorb, etc. When the experiments start, the concentration of CO is set up at a constant level of 175 ppm and the concentration of oxygen is altered in order to set up the desired gas mixtures in the flow (diluted in Ar), corresponding to different β-values. Before the experiments start we introduce a flow of oxygen diluted in Ar into the micro-flow reactor cell for 40 min. This procedure ensures that we start the experiments at $\beta = 0$, and also that we always start with oxidized CeO_x ($x \to 2$). A gas mixture corresponding to a low β-value is then introduced into the cell, and the gas mixture is then changed every 20 min to a new higher β-value (the typical time constant for reaching a new steady state point is $t \approx 1000$ s). This procedure is repeated until a high enough β-value is reached, i.e., until the transition to the low rate branch has occurred. The same procedure is then repeated, but with decreasing β-values in the gas mixture, until the transition to the high rate branch has been reached again. Typical traces for CO_2 production during CO oxidation are shown in Fig. 2 (filled circles) as the β-value is scanned low $\to$ high $\to$ low for all three samples (I–III), at a temperature of 450 K (simulations of the reaction kinetics is also shown in Fig. 2 (open squares) and will be commented on in Section 4).

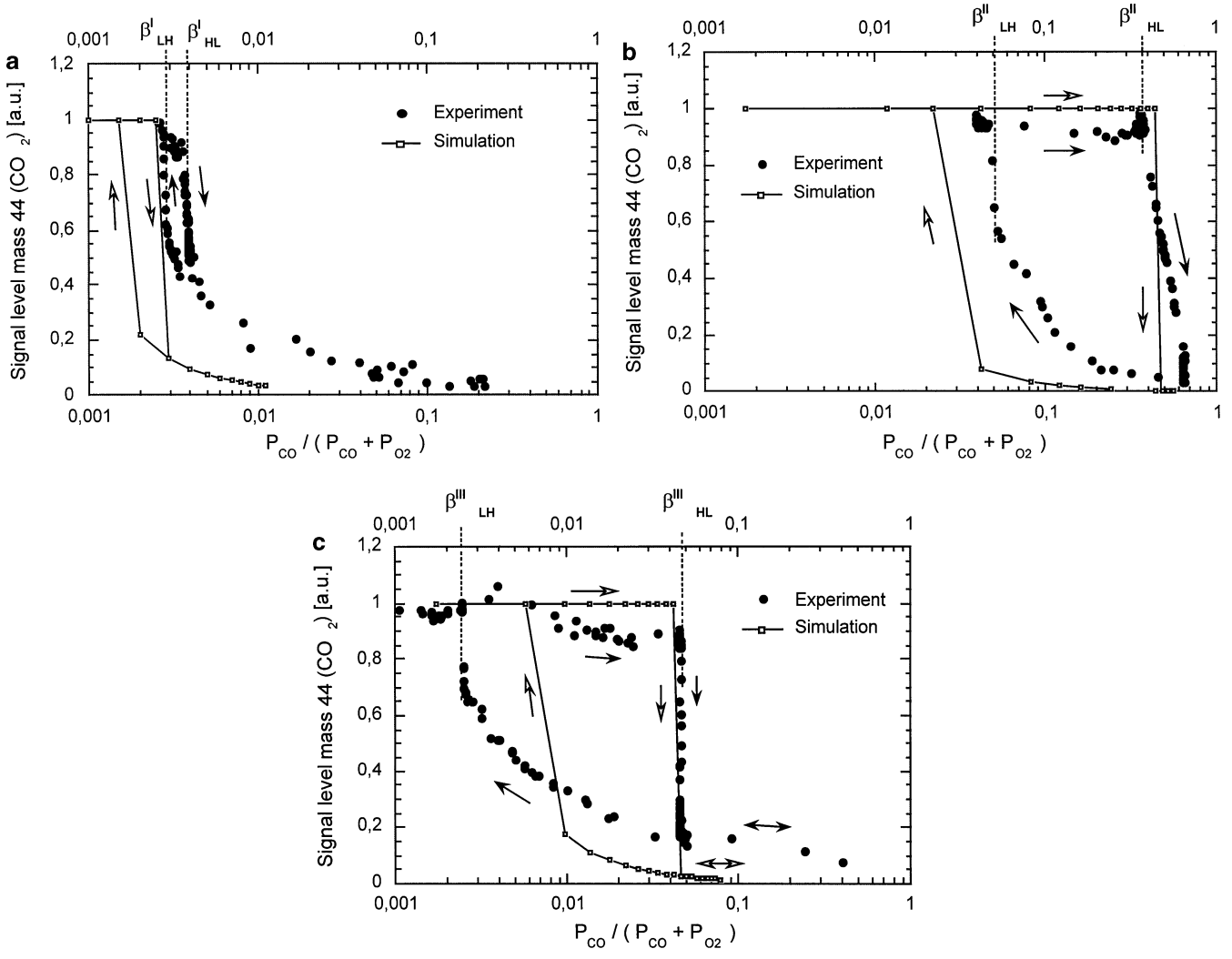

FIG. 2. The inlet gas mixture represented by the parameter $\beta \equiv P_{CO}/(P_{CO} + P_{O_2})$ has been scanned up/down at a constant temperature of 450 K, and the rate of CO_2 production has been monitored during the gas scan in β. This has been made for three different samples: (a) Pt/SiO_2 sample I, (b) Pt/CeO_x sample II, and (c) Pt/CeO_x sample III (disintegrated particles). Results both from experiments (filled circles) and gs (open squares) are shown. The β-values for the kinetic phase transitions between the high reaction rate branch (H) and the low reaction rate branch (L), and vice versa, are marked for the experimental data. The arrows indicate which reaction rate branch that has been observed while scanning up/down in β. A bistable region (hysteresis) is observed for all samples.

Note that the bistability region gives different β regimes for each sample, i.e., the kinetic bistability is sample dependent. Almost full conversion of CO is reached at low β-values and is maintained as the β-mixture is changed to higher values. As an example, for sample (III), the transition from the high rate branch (H) to the low rate branch (L) occurs at $\beta = 0.045$ (indicated by $\beta^{\mathrm{III}}_{\mathrm{HL}}$). The β-scan continues up to $\beta = 0.4$, at which point the β-value is decreased step-wise toward zero. When decreasing β, the rate is maintained at the low reaction branch at much lower β-values, compared with the transition from the high-to-low reaction branch. At $\beta = 0.0025$, the transition from the low to the high reaction branch occurs (indicated by $\beta^{\mathrm{III}}_{\mathrm{LH}}$). Plotted in this way, we thus find a hysteresis, or a bistable region, for which there exist two stable reaction points for each gas mixture (β-value). The CO_2 production trace, shown in Fig. 2c, thus has a bistable reaction region for β-values within $0.0025 < \beta < 0.045$. The β-values at which the bifurcation occurs are marked as follows in Fig. 2: $\beta^{\mathrm{I}}_{\mathrm{HL}}$, $\beta^{\mathrm{II}}_{\mathrm{HL}}$, and $\beta^{\mathrm{III}}_{\mathrm{HL}}$ for the transition from the high rate branch (H-branch) to the low rate branch (L-branch) for the samples (I–III), respectively, and as $\beta^{\mathrm{I}}_{\mathrm{LH}}$, $\beta^{\mathrm{II}}_{\mathrm{LH}}$, and $\beta^{\mathrm{III}}_{\mathrm{LH}}$ for the transition from the low rate branch to the high rate branch for samples I–III, respectively. In Fig. 2, it should be noticed that the former transitions ($\beta^{\mathrm{I}}_{\mathrm{HL}}$, $\beta^{\mathrm{II}}_{\mathrm{HL}}$, and $\beta^{\mathrm{III}}_{\mathrm{HL}}$) are separated by 1 order of magnitude for the three different samples. The bistability regions have been measured for a range of different temperatures, and for each EBL fabricated model catalyst sample (I–III). By collecting such bifurcation points at many different temperatures, a so-called bistability diagram (β vs T plot) can be obtained for each of the different samples (Fig. 3). These regions represent bistable regions in which two different stable reaction rate branches exist. In Fig. 3, it is seen that large differences are observed for the three samples (I–III) regarding (i) the absolute position of the bistable region in β-space, and (ii) the temperature interval at which the bistable region occurs. The most pronounced bistable region in Fig. 3 is observed for sample II, the nondisintegrated 750 nm Pt/CeO_x sample (cross-marked). A less pronounced bistable region is observed for sample III, the disintegrated 200 nm Pt/CeO_x sample (open squares). Sample I, the Pt/SiO_2 sample (filled dimonds with a dotted line), exhibits the smallest (narrowest) bistable region in Fig. 3.

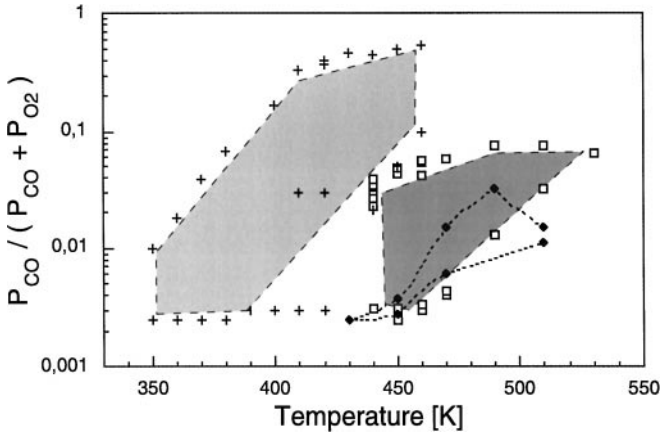

FIG. 3. Bistability diagrams are shown for Pt/SiO_2 sample I (filled diamonds with dotted line), Pt/CeO_x sample II (cross-marked; the bistable interval is shaded with lighter gray), and the Pt/CeO_x sample III with disintegrated particles (open squares; the bistable interval is shaded with darker gray). There are major differences observed both in temperature and in the β values for the bistability diagrams between the different samples. Note the logarithmic scale for the β value.

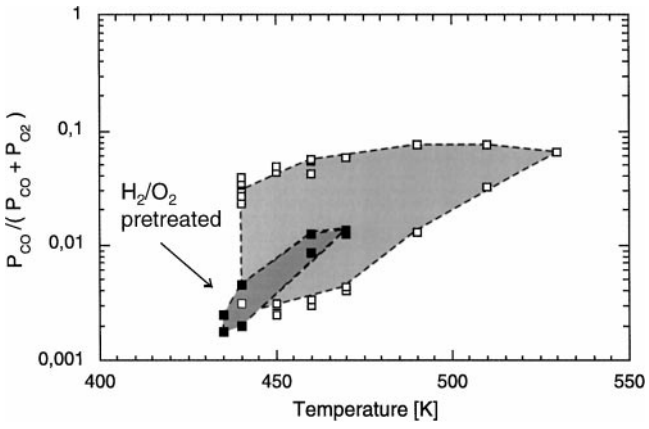

FIG. 4. Bistability diagrams for the Pt/CeO_x sample III (disintegrated particles) depending on the pretreatment. When pretreated for 1 h at 573 K in a 0.87% H_2 + 0.63% O_2 mixture diluted in Ar, a very narrow bistability diagram was observed (filled squares; bistable region shaded darker gray). After many runs without any H_2/O_2 pretreatment, the bistability diagram transforms into a wider bistability diagram (open squares; bistable region shaded lighter gray). The latter bistability diagram is also shown in Fig. 3.

If pretreated at 573 K for 1 h in a mixture of 0.87% H_2 + 0.63% O_2 diluted in Ar, the disintegrated sample III exhibits a much narrower bistability diagram (filled squares in Fig. 4). This narrow bistability diagram was found to be metastable, and it could be maintained for a few CO oxidation runs at different temperatures (<473 K) even without H_2/O_2 treatment in between. After many CO oxidation runs at different temperatures (<473 K and without H_2/O_2 treatments in between the runs), the very narrow bistability diagram transforms into a stable, wider (in β–T space), bistability diagram (open squares in Fig. 4). This latter bistability diagram is also plotted in Fig. 3. The very narrow bistability diagram for sample III can be reproduced by again pretreating the sample with the H_2/O_2 mixture at 573 K.

4. SIMULATIONS

To understand the qualitative behavior of the observed changes in the bistability diagrams as a function of particle size and support type, we have simulated the reaction kinetics including a reactant communication (spillover) channel

via the support. The idea is that oxygen can diffuse on the ceria support, providing an extra channel of oxygen supply to the Pt particles even at high CO partial pressures (high β-values), where the Pt particles otherwise would be CO poisoned. This mechanism should not be operative on Pt/SiO_2, and may therefore provide an explanation for the large differences between the 750 nm Pt/CeO_x and the 750 nm Pt/SiO_2 samples. In addition, the 200-nm Pt/CeO_x sample, which has a different Pt/CeO_x boundary length (per particle), gives us an opportunity to validate and quantify this mechanism.

To simulate the reaction kinetics occurring on Pt we employ the standard mean field approximation (23, 25), viz.

$$\begin{aligned}\frac{d\theta_{CO}}{dt} &= s_{CO}k^a_{CO}P_{CO} - k^d_{CO}\theta_{CO} - k^r\theta_{CO}\theta_O \\ \frac{d\theta_O}{dt} &= s_{O_2}k^a_{O_2}P_{O_2} - k^r\theta_{CO}\theta_O.\end{aligned} \qquad [4.1]$$

Here $s_{CO} = s^{(0)}_{CO}(1-\theta^2_{CO})$, and $s_{O_2} = s^{(0)}_{O_2}P_{00}(\theta_{CO},\theta_O)$ are the CO and O_2 sticking probabilities. The former expression yields a high sticking coefficient, with no O inhibition, up to very high CO coverage, which is in agreement with experiment (24). The latter expression describes the O_2 sticking, where P_{00} is the coverage dependent probability for an O_2 molecule to find two empty nearest-neighbor sites on the surface. The functional form of s_{O_2} should capture the CO inhibition and should have a much stronger influence on coverage than what is given by simple Langmuir adsorption (25). We have chosen s_{O_2} according to the quasi-chemical approximation (with a CO–CO repulsion of 4 kcal/mol) (27). This choice is, however, not important for the qualitative behavior of the solutions to Eq. 4.1. For the rate constants for CO desorption, K^d_{CO}, and CO + O reaction, k^r, respectively, we use the simplest mean-field expressions, with a linear dependence of the activation energies on the CO coverage (25).

$$k^d_{CO} = \nu^d_{CO}\exp(-(E^d_{CO} - A\theta_{CO})/kT) \qquad [4.2]$$

$$k^r = \nu^r\exp(-(E^r - B\theta_{CO})/kT). \qquad [4.3]$$

The mass transport equations consist of two contributions.

(i) A small gas flow ($\nu = 1$ μl/s) into the reactor volume. We employ a tank reactor model using 1 tank, which is sufficient since the residence time in the micro reactor is long compared to the gas mixing time in the reactor (see Section 2.2). The mass balance in the micro-flow reactor is then given by

$$v^{(i)}_{in} = vc^{(i)}_0 + W^{(i)}N_{Pt}, \qquad [4.4]$$

where N_{Pt} is the number of Pt particles, and $W^{(i)}$ is the reaction rate (per particle).

(ii) Diffusion from the gas bulk to the surface. We separate the solution to the diffusion equation into two regions. One far away from the sample and one near the Pt particles, which for simplicity is assumed to be half-spherical of radius R and with an interparticle spacing of $2L$. In the region far from the particles ($L \le z \le H$), at some distance H, which is macroscopic and large compared to all other distances, the gas concentration, $c^{(i)}$, of gas specie i, depends only on z, and the diffusion flux at $z = L$ per particle is given by

$$J^{(i)}_1 = 4D_{gas}L^2\left(c^{(i)}_0 - c^{(i)}_1\right)/(H-L), \qquad [4.5]$$

where c_0 is the bulk concentration and c_1 is the concentration at $z=L$, and D_{gas} is the diffusion coefficient in the gas mixture (which is almost equal for O_2 and CO (28)). In the simulations we take H to be the same as the reactor dimension. Near the Pt particles we assume that the solution to the diffusion equation is spherically symmetric around the particles $R \le r \le L$. With the boundary condition $c(L) = c_1$ and $c(R) = c_2$ the diffusion flux at $r = R$ is then given by

$$J^{(i)}_2 = 2\pi D_{gas}LR\left(c^{(i)}_1 - c^{(i)}_2\right)/(L-R). \qquad [4.6]$$

The diffusion flux toward the surface must be balanced by the reaction rate $W^{(i)}$, at $r = R$

$$W^{(i)}/i = \pi R^2 k^{(i)}_a c^{(i)}_2, \qquad [4.7]$$

where the stoichiometry factor is $i = 1$ for CO and $i = 2$ for O_2, and $k^{(i)}_a c^{(i)}_2$ is the net adsorption rate per unit area of reactant i. The balance equations relating Eqs. [4.5]–[4.7] are $J^{(i)}_1 = J^{(i)}_2$, and $J^{(i)}_2 = W^{(i)}$. Equations [4.1]–[4.7] are solved self-consistently and describe the mass transport coupled CO oxidation surface kinetics on the Pt particles.

Due to the small reactant flow into the reactor and the rapid CO + O reaction, the measured reaction response will be a convolution of the limited gas inlet flow, the bulk gas diffusion and the surface reaction kinetics. In fact, if the CO + O reaction rate and/or the number of Pt sites are sufficiently high, the solutions of Eqs. [4.1]–[4.7] may be completely determined by the limited gas supply to the reactor. It is therefore absolutely essential to know the number of Pt sites. We take advantage of the EBL method to prepare arrays of identical particles, and use SEM to estimate the geometrical area of the Pt particles (Table 1). In this manner we can fix the number of Pt sites on the EBL samples, which is crucial if one wants to explore and quantify the reaction kinetics, as described here. The reaction parameters for Pt only have been obtained by a least square fit to the experimental data for Pt/SiO_2 shown in Fig. 3 (β vs T), which we assume to behave as pure Pt particles with little influence from the support (29). In general, the simulated bistability diagram for the Pt/SiO_2 case exhibits a stronger dependence on the temperature than the experimental β vs T curve (which actually is decreasing at the highest between 490 and 510 K, as seen in Fig. 3). As a consequence, the fitted curve lies below the measured curve at

low T (as seen in Fig. 2a). A discussion of this point is given in Section 5. The reaction parameters have been chosen as fitting parameters because the interplay between the reaction rates, the net CO flux toward the surface, and the total reactant flow into the reactor is extremely sensitive for the exact location of the bistability region. The latter is accentuated by the very small inlet reactant flow, which provide very strong limitations on acceptable reaction parameters. The CO adsorption and desorption parameters, which are the parameters that are best known, have been chosen to correspond as close as possible to literature data (30–32). Far less is known about the CO + O reaction step (23), and therefore the parameters governing the CO + O reaction are allowed to be completely relaxed to fit the experimental data. The set of kinetic parameters that are used in our simulation is given in Table 1.

Following Zhdanov and Kasemo (26) the oxygen supply from the support to the Pt particles can be obtained by solving the diffusion equation describing the oxygen transport on the support. The rate of diffusion on the support to the Pt particles is then balanced by the rate of adsorption onto the support (K_{ad}) and desorption from the support (K_{des}), respectively. A net oxygen in-diffusion into the bulk is neglected, since we assume that we always have saturated (fully oxidized) CeO_x ($x=2$) due to the experimental procedures described in Section 3. Furthermore, we assume that the oxygen uptake is constant, independent of coverage, which is formally correct only if the oxygen coverage on the support, Θ, is small. It can be shown (33) that it is necessary to take into account the interference of the diffusion zones from adjacent particles, since the diffusion length on the support ($\sqrt{Dt}$) is larger than half the interparticle separation ($L_{1/2} = 325$ nm), under our experimental conditions (the experimental time constant is 1000 s for each steady state data point in Fig. 2). This is also consistent with available literature data (6, 7, 34, 35). Under these circumstances it is possible to obtain an approximate analytical form of the net flux of reactants from the support to the Pt particles, which facilitates the understanding of the support-mediated reactant supply (26). Assuming a single elementary jump rate for the reactant supply to (10) and from (01) the Pt particles, respectively, i.e., $K_{10(01)} = V_{10(01)} \exp(-E_{10(01)}/kT)$, the net O flux per Pt particle (per boundary site) is given by

$$k_{eff}\Theta(R) = (1-\theta)\Theta(R)K_{10} - K_{01}\theta, \qquad [4.8]$$

where $\Theta(R)$ is the oxygen surface coverage at the particle boundary $r=R$. An approximate solution to the diffusion equation together with Eq. [4.8] yields the following flux per site (per one particle)

$$F = \frac{2DP_{O_2}K_{10}K_{ad}(1-\theta)[1-K_{des}K_{01}\theta/K_{10}K_{ad}P_{O_2}(1-\theta)]}{R^2K_{des}[(1-\theta)K_{10}(\ln(L/R)+2D/K_{des}L^2)+D/aR]}, \qquad [4.9]$$

Here θ is the total surface coverage on Pt, D is the surface O diffusion constant, L is half the center-to-center distance between the Pt particles, and a is the lattice constant of the support. Equation (4.9) can be expressed in terms of the rate constants k^a_{CO}, k^d_{CO}, and $k^a_{O_2}$ describing the adsorption and desorption on Pt, which are interconnected via detailed balanced to K_{des} and K_{ad}. (Oxygen desorption from the support may in principle be neglected under our experimental conditions.) To describe the influence of a support-mediated channel given by diffusion of surface oxygen, Eq. [4.9] is simply added to the rate equation [4.1] for the oxygen coverage. This term may be viewed as an enhanced oxygen pressure, which approximately is given by

$$P^{eff}_{O_2} \approx \left(1+\frac{2DK_{10}}{R^2K_{des}(1-\theta)[(1-\theta)K_{10}(\ln(L/R)+2D/K_{des}L^2)+D/aR]}\right)P_{O_2}. \qquad [4.10]$$

Here we have f or clarity used a simple Langmuir form of

TABLE 1

Kinetic Parameters for CO Oxidation on Pt/Ceria and Pt/SiO_2 Used in the Simulations Shown in Fig. 2

CO adsorption on Pt
$k^a_{CO} = 1.9 \times 10^5$ mbar^{-1} s^{-1}
$s^{(0)}_{CO} = 0.84$

O_2 adsorption on Pt
$k^a_{O_2} = 3.6 \times 10^5$ mbar^{-1} s^{-1}
$s^{(0)}_{O_2} = 0.02$

CO desorption on Pt
$\nu^d_{CO} = 10^{14}$ s^{-1}
$E^d_{CO} = 38$ kcal/mol
$A = 15$ kcal/mol

CO + O reaction on Pt
$\nu^r = 3 \times 10^{11}$ s^{-1}
$E^r = 27$ kcal/mol
$B = 4.5$ kcal/mol

O diffusion on ceria
$\nu_{diff} = 10^{11}$ s^{-1}
$E_{diff} = 18$ kcal/mol

Attachment rate to (from) Pt particles from (to) ceria for O (CO)
$\nu_{10(01)} = 10^{12}$ s^{-1}
$E_{10(01)} = 30$ kcal/mol

O_2 desorption from ceria
$\nu_{des} = 10^{16}$
$E_{des} = 60$ kcal/mol

Number of surface Pt sites (from analysis of the SEM images in Fig. 1)
Sample I: 6×10^{12}
Sample II: 6×10^{21}
Sample III: 1.5×10^{12}

Diffusion coefficient in Ar (28)
$D_{gas} = 0.38$ cm^2/s

Micro-flow reactor inlet flow
$\nu = 10^{-3}$ cm^3/s

the oxygen adsorption to simplify the following discussion. This is sufficient to describe the main trends of Eq. [4.9], and does not change the qualitative conclusions. Furthermore, we have assumed that $k^a_{O_2} \approx K_{ad}$, which is reasonable. The major effect of including a reactant supply via the support (second term in Eq. [4.10]) compared to direct adsorption from the gas-phase on the Pt particles, is the much weaker coverage dependence of oxygen adsorption onto the support and subsequent (through diffusion) attachment to the Pt. The reported desorption temperature of oxygen from CeO_x varies considerably. It can be estimated that $E_{des} = 55$–65 kcal/mol, see, e.g., Refs. (6, 26, 35) and references therein. Similarly, the hopping barrier (E_{10}) is not well known (it is estimated that E_{10} is at least 24 kcal/mol), and a reliable value for the surface diffusion of oxygen is also lacking (7). With reasonable values of these parameters, we note, however, that Eq. [4.10] gives a significant contribution only if the second term in the denominator (which is large) is suppressed by the $(1 - \theta)$ term appearing within brackets (provided that D is sufficiently large), i.e., the particle must be close to O saturation. Otherwise, the relative oxygen contribution coming from the support is much smaller (independent of K_{10}, K_{des} , and D). The effect of the particle size (R) is to increase the effective boundary length. Thus a smaller particle will have a relative higher contribution coming from the support.

The simulated CO oxidation reaction, including an extra oxygen supply from the support (Eqs. [4.1]–[4.9]) in the case of ceria, describes very well the observed shifts in the bistability regions for the three different samples, considering the simplicity of the model. In Fig. 2 the results obtained at $T = 450$ K are shown (open squares). The emphasis in the simulations has been to adopt reported values for the kinetic rate constants for Pt as far as possible due to the fairly large particles sizes, and use as few free parameters as possible. Moreover, only the kinetic phase transition going from the high to the low reaction branch has been used to fit the experimental data, since the other kinetic phase transition (occurring at smaller β) was shown not to be as reliable from an experimental viewpoint (see Fig. 2). A comprehensive study, including the full simulations of all three sets of stability diagrams (β vs T) will be presented elsewhere (33). Here we present limits on the O surface diffusion and attachment rate that the spillover mechanism must obey in order to fit our experimental data. We find that $(E_{des} - E_{10}) > 25$–30 kcal/mol, with reasonable values for the prefactors, which gives a limit for $E_{10} < 30$–35 kcal/mol, using reasonable values for E_{des}, which is consistent with previous estimations made by Zhdanov and Kasemo (7) and provide for the first time an upper limit of the oxygen spillover energy barrier. The barrier for surface oxygen diffusion is estimated to be 15–20 kcal/mol with a prefactor of 10^{11} s^{-1}. This is consistent with the model of interfering diffusion zones, where the experimental conditions imply that $D > L^2_{1/2}/t = (325\text{ nm})^2/(1000\text{ s}) \approx 10^{-12}$ cm^2/s at $T = 450$ K. The parameters used in the simulations in Fig. 2 are shown in Table 1. To understand the result for the 200 nm Pt/ceria it is important to realize that the number of Pt sites is significantly lower for this sample (See Section 2.1), as measured by SEM (approximately by a factor of 4). The larger number of Pt particles present for the disintegrated 200 nm Pt/CeO_x sample, balance, however, the smaller number of Pt surface sites by increasing the relative boundary length (per particle), and hence the relative importance of the spillover effect. The total boundary length is in fact only decreased by ca. 2%, relative to the nondisintegrated samples. The result is a downshift of the bistable region down in β-space, relative to the nondisintegrated Pt/CeO_x sample (II). The exact position of the bistability region for the 200 nm Pt/CeO_x sample is well described using SEM data for the number of Pt sites and interface length, which provide further support for the oxygen diffusion model. It should be noted that without the oxygen supply channel present, the bistable region for the disintegrated Pt/CeO_x sample would be shifted even further down in β values than is the case for Pt/SiO_2, due to the much smaller number of Pt sites. In contrast, for the Pt/SiO_2 sample, which does not have this extra channel of oxygen supply, the bistable region is located at much lower β values.

5. DISCUSSION

This study shows that the EBL method may be used to fabricate well-defined model catalysts to measure, and discriminate between support-mediated and nonsupport mediated reactions, in a controlled way. These types of samples are well suited to use as model catalysts for simulation purposes, and can—as demonstrated here—provide very detailed information of the elementary reaction steps. We have thus prepared samples where the support is varied but all other parameters are kept the same (750 nm Pt/CeO_x, and $750/SiO_2$, respectively), and samples with different particle sizes on similar supports (750 nm Pt/CeO_x, and ca. 200 nm (mean size) Pt/CeO_2, respectively). The measured bistability diagrams (β vs T) for these three different samples are shown to be very different and are interpreted as being due to differences in the support type, and particle size, respectively. As shown in Section 4, this behavior can be quantitatively explained by introducing an additional oxygen reactant supply occurring via the ceria support in case of Pt/CeO_x, but not on Pt/SiO_2. A comparative study between Pt/CeO_x samples prepared with different size and interface length between the particles and ceria further supports these findings. The results provide some necessary conditions to be fulfilled for the support-mediated mechanism to be efficient. In the following we will discuss some important consequences of these findings.

The mobility of the O atoms on ceria, and the implication of this on the oxygen buffer capacity in car exhaust catalysts, have been recognized by many authors (1, 5–7). There is, however, very little quantitative information about the surface. In this work, we contribute to the understanding of the oxygen surface mobility and provide limits of the energetics of the oxygen diffusion and the spillover mechanisms. Note, however, that we cannot distinguish between the type of O diffusion mechanism, but merely derive limits for the effective O supply to the particle perimeter, whatever its origin may be. The simulated reaction kinetics shows that a support-mediated reactant supply channel is viable only if the barrier for an O atom to jump from the support onto a Pt particles is less than $E_{10} < 30$–35 kcal/mol. For our samples we find that the surface diffusion length ($\sqrt{Dt}$) on ceria must be larger than half the interparticle distance, i.e., 325 nm, implying that $D > 10^{-12}$ cm^2/s at $T = 450$ K. The simulations indicate that the effective oxygen diffusion barrier on CeO_x is $E_{diff} < 15$–20 kcal/mol. It is important to note that an O atom jumping from the support to the Pt particle, where it reacts with a CO molecule, is not the only scenario that can describe our experimental results. In fact, the phenomenological description of an oxygen jump process K_{10}, cannot be distinguished from a process where a CO molecule jumps over the boundary to react with an O atom that has diffused over the support to the particle boundary interface. The mathematical treatment (using the mean-field approximation) of this scenario would be analogous to that described in Section 4. However, it is still true within our model that O must diffuse on the support to become accessible for reaction at the particle boundary interface (via some activated process).

The inactivation of the Pt/CeO_x catalyst by H_2/O_2 treatment as described in Section 3, which is reversibly removed by prolonged CO oxidation, gives us further support of the oxygen surface diffusion model. It is likely that OH groups form on CeO_x and/or at the Pt/CeO_x interface during the H_2/O_2 treatment. It is known that OH groups are stable on CeO_x up to at least 673 K (36). This may have several different effects on the O spillover channel. It can either block interfacial Pt/CeO_x boundary sites, or it can block O adsorption on the support and/or the O surface diffusion on the support. The OH can, however, be removed by an oxidation treatment. Indeed, we have shown that the blocking of the spillover repeated CO oxidation (in oxygen excess) runs at temperatures below 473 K (Fig. 4) can remove the blocking of the spillover channel. The slow recovery at the lowest temperature indicates that the OH concentration at the surface is only slowly reduced under these conditions.

One important aspect of the experimental setup is that the reactant supply into the reactor is so small (10^{12} CO molecules/s) that the CO concentration in the reactor is (almost) depleted at the high reaction branch. The simulations show that this effectively shifts the bistability region for all samples to higher β-values. In this sense the micro-flow reactor can be viewed as a magnifying glass that shifts the bistability rigidly to higher β (compare, e.g., Ref. (23)). The transition from the low to the high reaction branch is therefore similar to a catalytic ignition in the sense that we are going from a regime where surface kinetics govern the reaction, to a regime where mass transport is dominant. The important difference is that here the rapid change in reaction rate is due to CO depletion in the reactor at constant temperature, and not due to thermal (i.e., exponentially growing) desorption of CO. The temperature increase of the sample due to the exothermic reaction can be shown to be negligible (due to a low total conversion of reactants). For the 750-nm Pt/ceria sample this also implies that the mechanism for going from the high to the low reaction branch can be completely determined by a limited gas-phase supply of oxygen when β becomes very high (O_2 pressure becomes sufficiently low). This is, however, not necessarily the case for the 200-nm Pt/ceria sample using the same condition, due to the smaller number of Pt sites on this sample. In this latter case the reaction rate cannot be sustained due to the surface reactions alone.

The measured bistability diagram on Pt/SiO_2 alone provides new data for the CO oxidation kinetics at atmospheric pressures *under conditions of oxygen excess*, which we have used to refine the rate parameters for CO oxidation. We obtain comparably low values for the reaction rate constant, especially the prefactor (Table 1), which yield a much lower reaction rate than some previous reports (24, 25, 37), while they are in good agreement with, e.g., Kaul *et al.* (38). Our choice of fitting the Pt reaction parameters to the Pt/SiO_2 data is guided by previous reports (29) of a more or less inactive SiO_2 support in the CO oxidation. Indeed we find it hard to reconcile our data with a very high CO reaction rate, k^r, even if possible scenarios where the SiO_2 is actively involved in the reaction scheme are considered. The reason follows. If the CO oxidation rate constants on Pt/SiO_2 are chosen so that the reaction rate becomes much higher, then a mechanism must be included to poison the reaction. Otherwise, it is not possible to go from the high to the low reaction branch when increasing β within our experimentally determined β region, since the limited CO reactant supply (via the micro-flow reactor and bulk diffusion) is effectively consumed by the high reaction rate. The O coverage is always close to saturation and the CO coverage is close to zero within the β region. One such poisoning mechanism could be, e.g., a CO supply from the SiO_2 support, which works in the opposite way as the O supply described above (26). However, to be able to explain the Pt/CeO_x data with the same high k^r, a similar "poisoning" mechanism must be operative in this case also, to keep the bistable region within our measured β window for Pt/CeO_x. The CO binding energies on the different supports are, however, in general too small to account for such a scenario at the

experimental conditions under consideration here (note that this condition is different from different CO binding energies at the Pt/support interface arising from differences in the particle–support adhesion (9)). Also, it should be noted that CO oxidation on the CeO_x support is not occurring in the T interval studied here as demonstrated on samples prepared with a CeO_x layer only. Another explanation of our fairly low reaction rate would be to ascribe our Pt particles to be less reactive due to some poisoning mechanism (e.g., by impurities) during fabrication. Our chemical analyses (AES and ESCA) of the EBL samples, do, however, not support such a mechanism. We therefore conclude that the effective CO oxidation rate, k^r, in an oxygen-rich environment is lower than on metal Pt at high pressures and temperatures if the surface reaction scheme used here is correct (Eqs. [4.1]–[4.3]). In analogy with previous suggestions (39–41) we propose that Pt may behave in a way similar to the other Pt metals (Pd, Rh) under these conditions, i.e., that a high pressure/temperature "oxidic" state may exist. The Pt metal is, however, expected to be more noble and indeed the "oxide" can be reversibly removed by fairly mild treatments (e.g., as described here). The existence of an oxidic state (with a concomitant lower effective reaction rate) may at least partly explain the discrepancy of the simulated β vs T stability diagram with the measured stability discussed in Section 4, where at higher T it is expected that oxidation is more severe (hence shifting down the bistability diagram in β). Possible extensions of the kinetic equations including an oxidic state may be incorporated in the analysis to remedy this discrepancy (39), but should not alter the qualitative conclusions of the work presented here. It is, however, worth noting that even after prolonged (several hours) exposures to O_2 at $T = 410$–530 K the measured reaction rate does not decrease significantly as we sweep β from low to high values on the high reaction branch (as described in Section 3). This would not have been the case if the formation of a surface oxide would be complete with an assumed zero sticking probability for CO adsorption on the oxide (40). If the $CO + O_2$ reaction on Pt is indeed low under the conditions discussed here it can have some interesting consequences that can be validated experimentally. It may imply, e.g., that the CO coverage at the high reaction branch is significant even at very low β values, far from the bifurcation point. By monitoring the CO frequency by FTIR spectroscopy one could test this proposition as β is swept across the bistable region.

CONCLUSIONS

We have demonstrated the usefulness of preparing well-defined model catalysts by EBL to study catalytic surface reactions. Samples with different support types and particle boundary lengths have been produced. We have in the case of Pt/ceria, shown that surface diffusion of oxygen on ceria to the Pt particles, followed by O (or CO) hopping to (from) the Pt particles explain the measured changes of the CO oxidation bistability region, as compared to Pt/SiO_2. For Pt/ceria a high reaction rate is maintained up to much higher β values (higher relative CO partial pressures) because of an extra O reactant channel sustaining full CO conversion. The role of the particle interface length has also been explored and shown to be important. The locations of the bistability regions (in β) are well described for all samples, by using a model with a minimum of free parameters. In particular, we take advantage of the EBL to prepare arrays of identical samples and use SEM to quantify the number of Pt sites and interface length. Estimates for the oxygen surface diffusion on ceria and the activated jump (or reaction) process occurring at the Pt/ceria interface have been obtained. These are in good agreement with previous estimates. The influence of Pt oxidation in the CO oxidation in oxygen excess is discussed in terms of a less reactive (oxidic) Pt state.

ACKNOWLEDGMENTS

This study was performed within the Competence Centre for Catalysis, which is financially supported by the Swedish National Energy Administration and by the member companies: AB Volvo, Johnson Matthey CSD, Saab Automobile AB, Perstorp AB, Eka Chemicals AB, and MTC AB.

REFERENCES

1. Farrauto, R. J., and Hech, R. M., *Catal. Today* **51**, 351 (1999).
2. Taylor, K. C., *Catal. Rev. Sci.* **35**, 457 (1993).
3. Serre, C., Garin, F., Belot, G., and Maire, G., *J. Catal.* **141**, 1 (1993).
4. Zafiris, G. S., and Gorte, R. J., *J. Catal.* **139**, 561 (1993).
5. Muraki, H., and Zhang, G., *Catal. Today* **63**, 337 (2000).
6. Holmgren, A., Duprez, D., and Andersson, B., *J. Catal.* **182**, 441 (1999).
7. Zhdanov, V. P., and Kasemo, B., *Appl. Surf. Sci.* **135**, 297 (1998).
8. Poppa, H., *Catal. Rev. Sci. Eng.* **35**(3), 359 (1993).
9. Henry, C. R., *Surf. Sci. Rep.* **31**, 231 (1998).
10. Gunter, P. L. J., Niemantsverdriet, J. W., Riberio, F. H., and Somorjai, G. A., *Catal. Rev. Sci. Eng.* **39**(1/2), 77 (1997).
11. Heiz, U., and Schneider, W.-D., *J. Phys. D: Appl. Phys.* **33**, R85 (2000).
12. Kuipers, E. W., Laszlo, C., and Wieldraaijer, W., *Catal. Lett.* **17**, 71 (1993).
13. Hanarp, P., Sutherland, D., Gold, J., and Kasemo, B., *Nanostruct. Mater.* **12**, 429 (1999).
14. Pileni, M. P., *Langmuir* **13**, 3266 (1997).
15. Wong, K., Johansson, S., and Kasemo, B., *Faraday Discuss.* **105**, 237 (1996).
16. Johansson, S., Wong, K., Zhdanov, V. P., and Kasemo, B., *J. Vac. Sci. Technol. A* **17**(1), 297 (1999).
17. Jacobs, P. W., Riberio, F. H., Somorjai, G. A., and Wind, S. J., *Catal. Lett.* **37**, 131 (1996).
18. Johansson, S., Fridell, E., and Kasemo, B., *J. Vac. Sci. Technol. A.* **18**(4), 1514 (2000).
19. Ertl, G., *Adv. Catal.* **37**, 231 (1990).
20. M. Bardau *et al., J. Chem. Phys.* **110**, 11,551 (1999).
21. Zhdanov, V. P., and Kasemo, B., *Surf. Sci. Rep.* **20**, 111 (1994).
22. Garske, M. E., and Harold, M. P., *Chem. Eng. Sci.* **47**(3), 623 (1992).
23. Zhdanov, V. P., and Kasemo, B., *Appl. Surf. Sci.* **74**, 147 (1994).

24. Bär, M., Zulicke, C., Eiswirth, M., and Ertl, G., *J. Chem. Phys.* **96**(11), 8595 (1992).
25. Rinnemo, M., Kulginov, D., Johansson, S., Wong, K. L., Zhdanov, V. P., and Kasemo, B., *Surf. Sci.* **376**, 297 (1997).
26. Zhdanov, V. P., and Kasemo, B., *J. Catal.* **170**, 377 (1997).
27. Zhdanov, V. P., "Elementary Physicochemical Processes on Solid Surfaces." Plenum Press, New York, 1991.
28. Marrero, T. R., and Mason, E. A., *J. Phys. Chem. Ref. Data.* **1**(1), 3 (1972).
29. Xu, X., and Goodman, W. D., *J. Phys. Chem.* **97**, 7711 (1993).
30. Seebauer, E. G., Kong, A. C. F., and Schmidt, L. D., *Surf. Sci.* **176**, 134 (1988).
31. Szabo, A., Kiskinova, M., and Yates, J. T. J., *J. Chem. Phys.* **90**, 4604 (1989).
32. Ertl, G., Neumann, M., and Streit, K. M., *Surf. Sci.* **64**, 393 (1977).
33. Österlund, L., Johansson, S., and Kasemo, B., submitted for publication.
34. Martin, D., and Duprez, D., *J. Phys. Chem.* **100**, 9429 (1996).
35. Putna, E. S., Vohs, J. M., and Gorte, R. J., *Catal. Lett.* **45**, 143 (1997).
36. Badri, A., Binet, C., and Lavalley, J.-C., *J. Chem. Soc. Faraday Trans.* **92**(23), 4669 (1996).
37. Herz, R. K., and Marin, S. P., *J. Catal.* **65**, 281 (1980).
38. Kaul, D. J., Sant, R., and Wolf, E. E., *Chem. Eng. Sci.* **42**, 1399 (1987).
39. Sales, B. C., Turner, J. E., and Maple, M. B., *Surf. Sci.* **147**, 381 (1982).
40. Dicke, J., Rotermund, H. H., and Lauterbach, J., *Surf. Sci.* **454–456**, 352 (2000).
41. Matsushima, T., Almy, D. B., and White, J. M., *Surf. Sci.* **67**, 89 (1977).